actuators

MDPI

Article

Non-Crack-Growth Acoustic Emission Observed in Controlled-Stress-Intensity-Factor High-Cycle-Fatigue Tests

Roshan Joseph [1,*] and Victor Giurgiutiu [2]

[1] Acellent Technologies Inc., Sunnyvale, CA 94085, USA
[2] Department of Mechanical Engineering, University of South Carolina, Columbia, SC 29208, USA
* Correspondence: 4roshanj@gmail.com

Abstract: Acoustic emission (AE) was monitored during stress intensity factor (SIF)-controlled high-cycle fatigue (HCF) tests on an aluminum 2024-T3 specimen with a fatigue crack growing at its center. The SIF control was implemented in such a manner that crack growth could be slowed down and even inhibited while the fatigue experiment continued. In the beginning, a specific type of AE signal was observed while the crack was allowed to grow to up to approximately 9.4 mm in length. Subsequently, the load was reduced in order to control the SIF value at the crack tip and to inhibit the crack growth. AE signals were recorded even when the crack stopped growing, although the specific signature of these AE signals was different from those observed when the crack was growing, as discussed in the text. The gist of the phenomenon reported in this article is that strong AE signals could still be observed even when the crack stopped growing. These latter AE signals could be due to rubbing and clapping of the crack faying surfaces. Travel analysis was consistently performed to ensure that these AE signals were originating from the crack, though not necessarily from the crack tip. In addition, absorbing clay wave dams were built around the crack region to inhibit boundary reflections and grip noise. Fast Fourier Transform (FFT) and Choi–Williams Transform (CWT) analysis were performed to classify the AE signals. It was observed that the AE signals related to crack growth were clearly different from the AE signals originating from the crack while the crack was not growing. Strong S0-mode Lamb wave components were observed in the crack-growth AE signals, whereas strong A0-mode Lamb wave components dominated the non-crack-growth AE signals. Pearson correlation clustering analysis was performed to compare the crack-growth and non-crack growth AE signals. We propose that the fatigue-crack faying surfaces may undergo rubbing and/or clapping during fatigue cyclic loading and thus produce strong AE signals that are registered by the AE system as hits, although the crack is not actually growing. The understanding of this phenomenon is very important for the design of the structural health monitoring (SHM) system based on AE-hit signal capture and interpretation.

Keywords: structural health monitoring (SHM); acoustic emission (AE); stress intensity factor (SIF); high cycle fatigue (HCF) experiment; AE signal mode separation; crack rubbing/clapping AE

check for updates

Citation: Joseph, R.; Giurgiutiu, V. Non-Crack-Growth Acoustic Emission Observed in Controlled-Stress-Intensity-Factor High-Cycle-Fatigue Tests. *Actuators* **2023**, *12*, 93. https://doi.org/10.3390/act12030093

Academic Editor: Hongli Ji

Received: 30 December 2022
Revised: 11 February 2023
Accepted: 13 February 2023
Published: 21 February 2023

1. Introduction

The growing number of aging engineering structures and the variable working conditions demand more from the scientific community for a staunch and scrupulous technology for health monitoring purposes. The AE analysis method is a well-known structural health monitoring (SHM) and non-destructive testing (NDT) technique. The AE analysis method has been commonly used as passive sensing of signals during a damaging process. However, AE analysis has also been used in active mode by actively inducing AE into the structure and analyzing its scattering characteristics. The AE method principle is the detection of elastic waves originating from a damage or energy release process. The damage or energy release process in metallic structures is crack propagation, plastic deformation [1], impact hit, rubbing/clapping of an existing crack surface, etc. The elastic waves generated due to the AE source in the ultrasound band are sensed using AE sensors. If properly designed, such SHM systems can allow more endurance to the engineering structures. A passive AE-SHM system integrated with an active SHM inspection system is the best solution for an ideal health monitoring system. Offshore wind turbines, aircrafts, bridges, naval structures, etc., will receive the most benefit of such SHM systems since their maintenance downtime represents a large part of their operating cost.

The AE technique has been used for damage detection and source localization of fatigue crack growth in metallic structures. The AE method is a passive, wave-propagation-based SHM method for in situ monitoring. The study of acoustic emission during a fatigue crack-growth event has attracted many researchers over time. Many researchers have studied the AE due to fatigue crack growth as well as wave scattering from fatigue cracks [2–7]. Zhang et al. [1] studied the acoustic emission signatures of fatigue damages in an idealized bevel gear spline and identified two different AE signal signatures for plastic deformation and crack jump. Bhuiyan et al. [8–10] studied the AE signal signatures recorded by PWAS transducers during a fatigue crack growth experiment in thin metallic plates. In this research, under a slow frequency of fatigue loading (<0.25 Hz), for a short advancement of crack length, the AE signals were recorded, and eight signal signatures were discovered related to crack growth and crack rubbing and clapping. Hamstad and McColskey [11] studied the detectability of slow crack growth AE in a fatigue experiment. In this research, a 0.3 Hz cyclic fatigue loading was applied on 1-inch-thick steel and aluminum specimens. The experiment was performed by controlling the crack growth rate by maintaining a fixed range of stress intensity factor (ΔK) with fixed minimum and maximum loads. This method achieved very slow fatigue crack growth rates for the 1×10^{-4} mm/cycle and 1×10^{-3} mm/cycle. Four resonant sensors and four wideband sensors were used for recording AE signals. Through waveform inspection, crack events were separated from the grip events. It was found that the use of wideband sensors can enhance the ability to make the necessary distinction of AE signals during a fatigue experiment. The manuscript has been updated with the corresponding reference. Roberts and Talebzadeh [2] discussed the correlation between acoustic emission count rates and crack propagation rates. Various signal processing methodologies and clustering techniques have been used to differentiate AE signals due to various activities [12]. The correlation between crack characteristics and AE signal features has also been analyzed using different techniques [13–16]. Researchers have used the clay boundaries very effectively to prevent the reflection of waves from the plate boundaries during ultrasonic experiments. Clay boundaries have been used during the pitch-catch experiment for damping the reflections from boundaries [17]. Clay boundaries have been used for reducing reflections from AE during a low cycle fatigue experiment [8]. A FEM numerical study of providing damping at the boundaries of a plate to prevent boundary reflection was also studied [18].

The theoretical studies of AE and experiments were performed by many researchers to understand the underlying principles of AE, the source mechanism, and used those understandings for AE simulations. These studies helped to understand the AE signal signature and AE source mechanism in both theoretical and experimental perspectives. A generalized theory of AE and AE-source-mechanism representations for a half-space was developed by Ohtsu and Ono [19]. Ohtsu and Ono further continued the work by performing the simulation of tensile crack and shear crack in half-space [20]. This paper describes how significant the AE source mechanism is in forming the AE signal characteristics. Finite element modeling works performed by Hamstad, Sause, and Prosser showed how the Lamb wave propagation in plates happens due to an AE activity [21–24]. Wisner and Kontsos [25] performed direct particle observations coupled with simultaneous AE, which enabled the identification of AE features that could be related to particle fracture during cyclic loading conditions. Wisner et al. [12] performed in situ experiments to link AE signals with a particular damage mechanism. In this research, the clustering of AE signals was performed based on various source mechanisms. One of the significant scopes of the present research work is to understand the AE signals in thin metallic plates based on the source mechanisms.

The AE signal features such as duration, rise time, counts frequency contents, etc. are strongly dependent on the characteristics of the physical phenomenon that generated the AE signal [26]. Several studies have utilized AE measurements to identify the corresponding fracture mechanisms [27,28]. Time-frequency domain-based approaches and modal separation approaches were used for this purpose. AE measurement time-domain features are strongly affected by experimental conditions, whereas frequency content is not changed [29].

Many researchers used time-frequency representations of the AE signals for distinguishing the signal types. Suzuki et al. [30] used the wavelet transform for analyzing the AE signals from a longitudinal glass-fiber reinforced composite sample under tensile loading. The authors analyzed the AE signals recorded using piezo patches and classified the signals into four types using the wavelet transform method. This research performed the correlation of signal types to Mode-I fiber fracture, Mode-I matrix crack, and Mode-II disbonding. Many researchers proved the time-frequency transform technique to be a useful tool for AE signal analysis [31–33]. In the present paper, we have used both frequency spectrum analysis as well as time-frequency decomposition analysis of AE signals for AE signal characterization.

Various AE sensors have been used for the detection of AE signals; in particular we use R15a [34] and S9225 [35] from Physical Acoustics Corporation. R15a is a resonant sensor with a resonance frequency of 150 kHz, whereas the S9225 is a wideband sensor with a comparatively small size. Various types of resonant and wideband AE sensors are available these days. Fiber optic sensors such as fiber Bragg grating (FBG) AE sensors have high sensitivity and small size. However, the FBG sensor performance is affected by the sensor's directional sensitivity [36–38]. The piezoelectric wafer active sensors (PWAS) are commonly used these days for the detection of AE signals. PWAS transducers have several excellent characteristics, such as high sensitivity and good stability [39]. In this research, two PWAS transducers and two S9225 sensors were used for the recording AE signals. These sensors were placed symmetrically on either side of the crack, one close to the crack, and the other further away.

The essence of this paper is to report and discuss the fact that strong AE-hit signals can be recorded by the AE monitoring system even when the crack stops growing. The authors had the intuition that something of importance may be there, especially that in other related work, we observed that cracks emit kHz-range AE signals when they are vibrated transversely at Hz range frequencies [40]. Those kHz-range AE signals were explained as being due to microfractures taking place during rubbing or clapping of the crack faying surfaces due to Hz-range vibration. When examining the frequency spectra or the AE signals collected in the current work, we observed that some of the spectra seem similar to those emitted by fatigue crack subjected to lateral vibration, whereas others did not. It became apparent that the signals which were similar to our previous observation reported in [40] were due to some rubbing or clapping of the crack faying surfaces during the cyclic axial loading applied in the fatigue experiment (The crack faying surfaces are not perfectly plane and clean, but inclined and with pronouncing asperities, as proven by micrographic examination). Several investigators have posited that the AE signals captured during the AE monitoring contain a wealth of information that is not properly exploited by the current AE practice which is solely based on counting "hits". To overcome this, some authors have taken a data-driven approach and applied statistical signal processing to extract standardized signal features such as amplitude, rise time, duration, MARSE (measured area of the rectified signal envelop), counts, moments, kurtosis, "signal energy", etc. [41,42]. The success of these methods still depends a lot on being able to discard the AE signals not related to crack growth. The differentiation of propagating crack AE signal and non-crack growth AE signal is very important for understanding if the AE signal generated is due to crack growth or not. This differentiation has long term future advantages of identifying crack length from the AE signals. The present research has differentiated the AE signals related to crack growth and crack rubbing/clapping. The crack rubbing/clapping AE signals were generated even without crack growth. However, the crack-growth-related AE signals were observed when a crack growth happened. Therefore, the identification of non-crack growth fatigue crack rubbing/clapping signals is important for understanding if there is a crack growth happened or not from the signal signatures. To achieve this type of measurements, we developed a SIF-controlled fatigue-testing methodology that was applied here to control and even inhibit the crack growth after a certain crack length was attained. Consistent AE monitoring was implemented throughout the experiment. Post-processing of the recorded AE signals, performed with Fast Fourier Transform and Choi–Williams transform, revealed clear differences between the AE signals recorded during crack growth and the AE signals recorded later in the experiment when the crack was no longer growing. The article is organized as follows: the experimental setup of the fatigue AE experiment is presented in Section 2, which describes the specimen preparation, sensor instrumentation, and AE experimental setup. In this section, the novel concept of the SIF-controlled AE experiment is also described. Section 3 contains the AE experiment results and discussions. The results of the novel SIF-controlled AE experiment and its interpretation are presented in Section 3.2. This paper ends with a summary, conclusions, and suggestions for further work.

2. Experimental Set-Up

2.1. Specimen Preparation

An AE experimental specimen was designed for capturing AE during crack growth in thin metallic plates. Aluminum 2024-T3, a commonly used aircraft material, was chosen for preparing the test specimens. From a large plate of aluminum 2024-T3, coupons of 103 mm width, 305 mm length and 1 mm thickness were machined using the shear metal cutting machine. Specimens were sufficiently wide enough to allow a long crack form in the specimen. Fatigue cyclic loading was performed on the specimen by applying fatigue load ranging from 13.85–1.38 kN at 10 Hz. A fatigue crack was originated from the hole due to the continuous fatigue loading. The tip-to-tip crack length was 4 mm at 322 kcycles of fatigue loading. When the crack initiation happened, the specimen was taken out of the MTS machine. The sensors were installed, and a non-reflective clay boundary (NRB) was implemented on the specimen. The NRB was applied to the specimen to prevent AE signal reflections from the plate boundaries and thus to receive reflection-free, clean AE signals. After the AE sensor and NRB implementation on the specimen (Figure 1), the crack had grown by an additional 5.4 mm (until the crack length reached 9.4 mm tip to tip), simultaneously capturing the AE signals. The specimen's wide geometry was desired for this work so that the acoustic waves generated would travel a longer distance to the edges. This hypothesis, in turn, means the signals die out after reflection from the boundaries due to geometric spreading and material damping before reaching the sensors. The properties of Al 2024-T3 were: modulus of elasticity 73 GPa, density 2767 kg/m^3, and Poisson's ratio 0.33.

2.2. Sensor Instrumentation for AE Recording

Two PWAS sensors and two S9225 sensors were bonded to the aluminum specimen. PWAS sensors were bonded at a distance of 6 mm and 25 mm from the crack in a linear configuration. S9225 sensors were bonded to the specimen at 6 mm and 25 mm from the crack in the opposite direction to the PWAS sensors. The specimen bonded with sensors is presented in Figures 1 and 2. PWAS sensors were bonded using M-Bond AE-15 adhesive. This adhesive is appropriate for bonding PWAS because it is resilient to the dis-bonding of PWAS during extended durations of cyclic loading. M-Bond AE-15 is an epoxy system with two components, a resin, and a curing agent. The resin and curing agent were mixed in a specific proportion and stirred for 5 min. This mixture was used to bond the PWAS to the specimen. The PWAS was bonded to the specimen using the mixture and cured for

3 h at 600 C as recommended by the epoxy manufacturer. The capacitance of the PWAS was measured before bonding and after bonding. The capacitance values made sure that the PWAS and the bonding to the specimen were defect-free. The two S9225 sensors were bonded to the specimen using hot glue. A drop of hot glue was applied to the specimen using a heat gun, and the sensors were placed on the drop with the application of thumb pressure. The thumb pressure was applied continuously until the hot glue was cured.

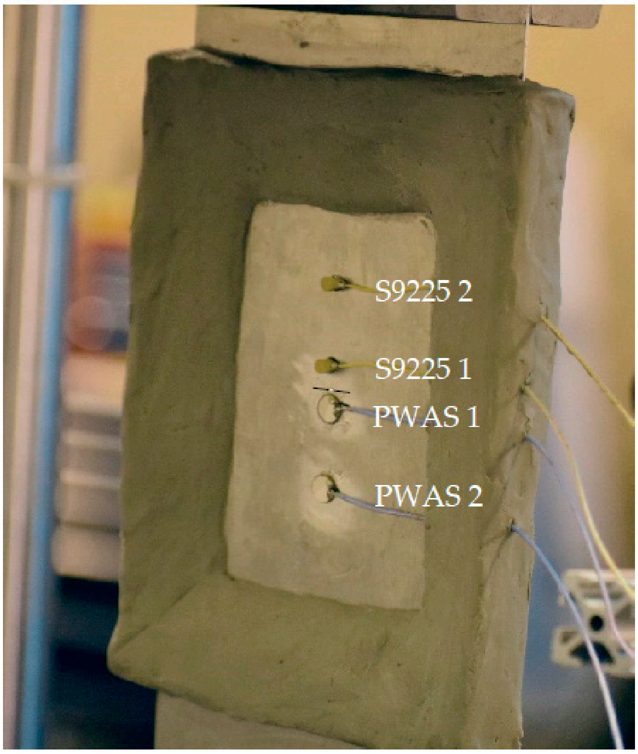

Figure 1. AE test specimen bonded with the two-PWAS and two-S9225 sensors. Non-reflective clay boundaries (NRB) were provided on the specimen to avoid the reflection of AE signals from the specimen boundaries.

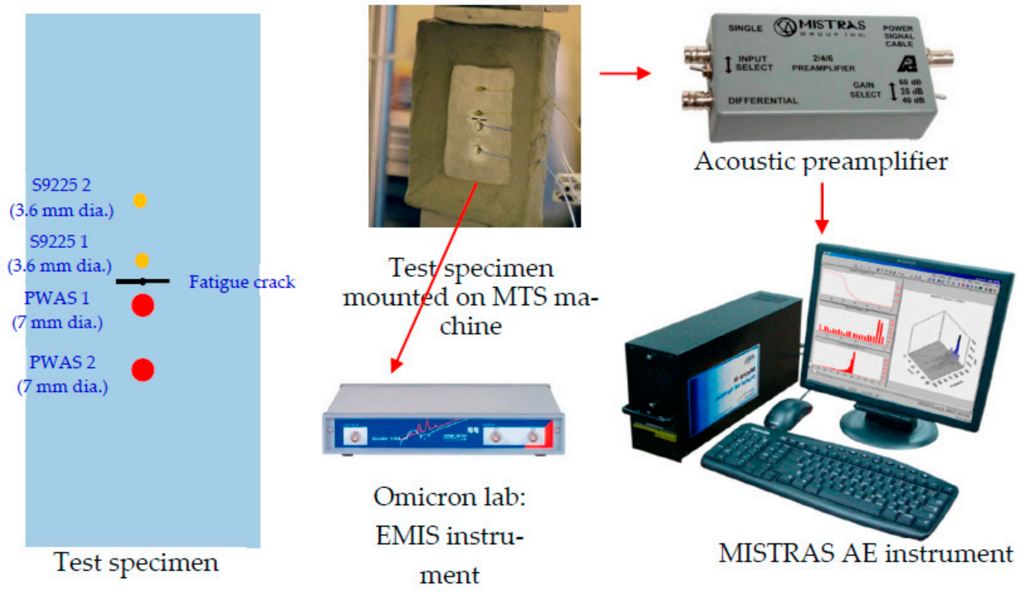

Figure 2. Experimental setup for capturing AE signals during fatigue crack event.

2.2.1. PWAS Transducers

Piezoelectric wafer active sensors (PWAS) are inexpensive, lightweight, small, and unobtrusive transducers that work on the piezoelectric principle. PWAS are available in different geometries and dimensions. They can be permanently bonded to a structure to transmit and receive guided waves. The PWAS transducer couples the electrical and mechanical effects. The PWAS sensing mechanism is presented in Figure 3. The PWAS senses the in-plane and out-of-plane wave motions through sensing the in-plane strain. The sensing equation of a PWAS transducer in tensor notation is written as follows:

$$\begin{array}{l} \text{Electric field at PWAS, } E_i = -g_{ikl}\sigma_{kl} + \beta^T_{ik} D_k \\ \text{Strain at PWAS, } S_{ij} = s^D_{ijkl}\sigma_{kl} + g_{kij} D_k \end{array} \tag{1}$$

where E_i is the electric field at PWAS, S_{ij} is the strain at PWAS, D_k is the electric displacement, g_{ikl} is the piezoelectric voltage coefficient, σ_{kl} is the stress on the PWAS, $\beta^T{}_{ik}$ is the impermittivity coefficient, $s^D{}_{ijkl}$ is the compliance. The method of operation of the PWAS transducer element depends on the polarization of the PZT (lead-zirconate-titanate) during the manufacturing process. In this research, the PWAS transducer of 7 mm diameter and 0.5 mm thickness, polarized in d_{31} operation mode, was used for AE sensing. Such a polarization enables the PWAS to sense the in-plane strain (along 1-direction) and produce an electric voltage in the thickness direction (along 3-direction), E_3. The response of a PWAS during AE sensing depends on the tuning of the Lamb wave on the PWAS. The experimental tuning curve (Ref. [1], p. 620) of the PWAS sensor on a 1 mm aluminum plate was generated and presented in Figure 4b. In the tuning curve of the PWAS sensor, we observe the normalized voltage response of the PWAS sensor at various frequencies. The S0 and A0 Lamb wave mode contributions in the tuning have been marked blue and red squares, respectively, in the plot. In the experimental result, a rejection point was observed for A0 mode at around 300 kHz. On the other hand, a strong response of A0 mode was observed at around 50 kHz. A strong S0 mode response was also observed at around 430 kHz. The theoretical A0 and S0 Lamb wave tuning curve [1] for 7 mm PWAS on a 1 mm aluminum plate is also presented in Figure 4b. As we observe, the experimental results are matching well with the theoretical prediction.

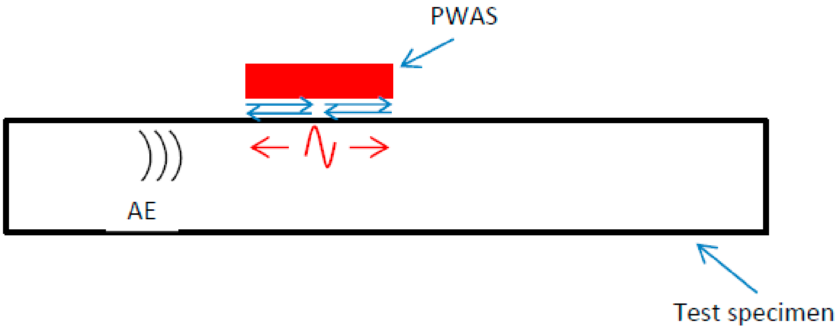

Figure 3. PWAS sensing mechanism. PWAS senses in-plane and out-of-plane wave motions through sensing in-plane strain.

2.2.2. S9225 AE Sensor

A schematic of a typical AE sensor is presented in Figure 5. An AE sensor's major components consist of a piezoelectric element, wear plate, damping material, and a case. The top electrode of the piezoelectric element is connected to the connector, and the bottom surface is grounded to the case of the AE sensor and bonded to the wear plate through an electrically conducting bond. The components of the AE sensor are secured inside the case. A couplant is used to bond the AE sensor to the specimen in which the AE measurement needs to be performed.

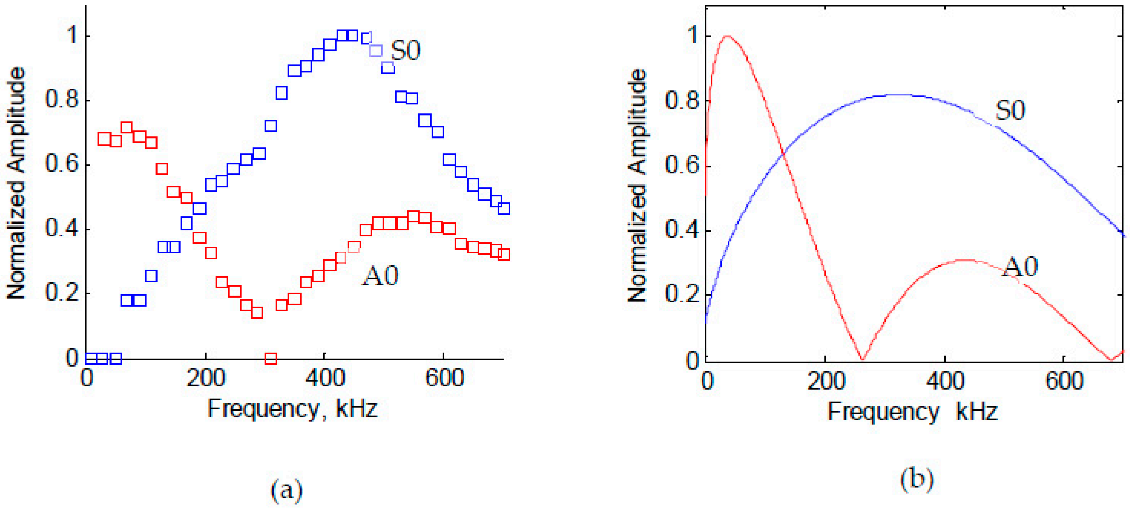

Figure 4. The Lamb wave tuning of 7 mm round PWAS on 1 mm 2024-T3 aluminum plate: (**a**) experimental results; (**b**) theoretical prediction.

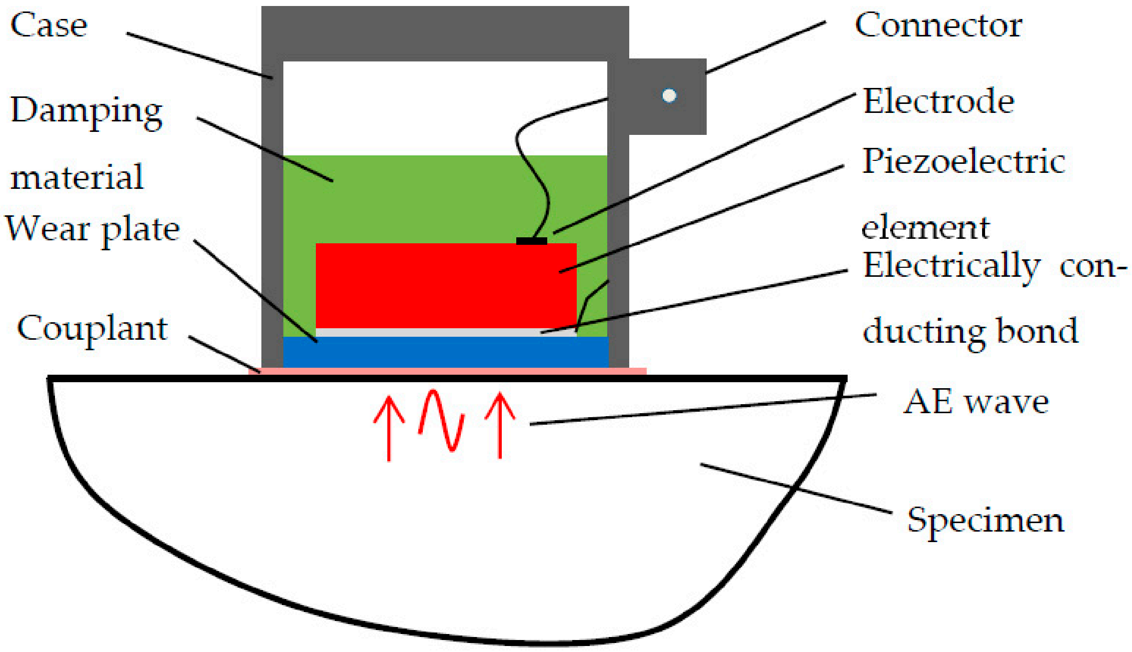

Figure 5. Schematic of a typical AE sensor.

Acoustic emission sensors respond to dynamic motion caused by an AE event. The transducer element in the AE sensor converts mechanical movement into an electric voltage signal. In general, the commercial AE sensors measure the pressure applied on the sensor's surface due to the velocity of the surface particle of the specimen [43]. Commonly, the transducer element is a piezoelectric crystal made from ceramic such as lead-zirconate-titanate (PZT). The transducers are sensitive to the out-of-plane motion of the acoustic wave signals [44]. AE sensors are generally classified into two broad classes based on their operating frequency: resonant and broadband. In the present experiment, we have used the S9225 AE sensor, which operates in broadband. The frequency response spectrum of S9225 sensor is presented in Figure 6.

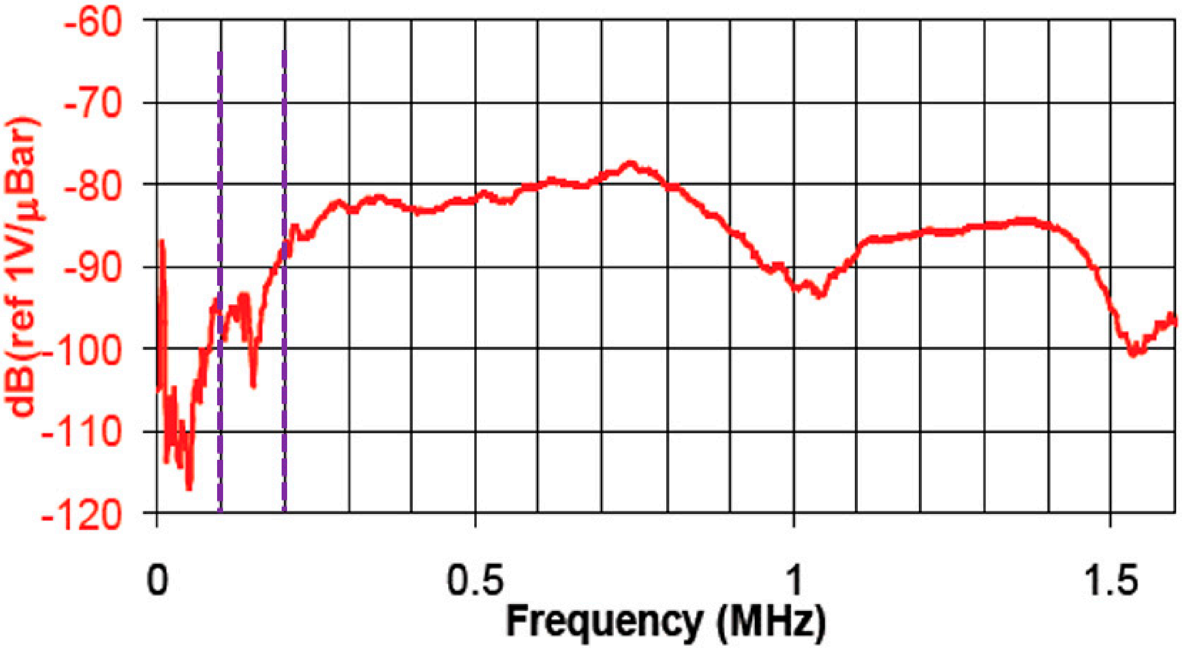

Figure 6. Frequency response of S9225 sensor from the manufacturer.

2.3. AE Experimental Setup

After installing the sensors, the fatigue loading was continued to grow the crack and capture AE signals simultaneously. The test specimen installed with PWAS and S9225 transducers was mounted on the MTS machine (Figure 1). The experimental setup for capturing the AE signal from a fatigue crack growth event is presented in Figure 2. The bond quality assurance of PWAS sensors was performed periodically by electromechanical impedance spectroscopy (EMIS). AE signals during crack growth events were captured by using PWAS and S9225 sensors. The sensors were connected to the acoustic preamplifier. The acoustic preamplifier is a bandpass filter that filters out signals between 30 kHz and 700 kHz. Provided with 20/40/60 dB gain (can be selected using a switch), this preamplifier operates with either a single-ended or differential sensor. In the present experiment, 40 dB gain was selected. The preamplifier was connected to the MISTRAS AE system. A sampling frequency of 10 MHz was chosen to capture any high-frequency AE signals. The timing parameters set for the MISTRAS system were: peak definition time (PDT) = 200 µs, hit definition time (HDT) = 800 µs, and hit lockout time (HLT) = 1000 µs.

2.4. Electro-Mechanical Impedance Spectroscopy (EMIS) Sensor Integrity Check

The PWAS was bonded to the specimen using M-Bond AE-15. Continuous fatigue loading can cause the damage of PWAS or dis-bonding of the PWAS from the specimen. The dis-bonding of the PWAS would cause the capturing of false AE signals. To monitor the condition of PWAS during the fatigue experiment, we have used EMIS inspection periodically during cyclic fatigue loading [45]. The results of EMIS measurements are presented in Figure 7. No considerable change in EMIS measurements was observed for PWAS 1 and PWAS 2. The EMIS measurement confirmed that no false AE signals were recorded by the PWAS during the fatigue crack growth event.

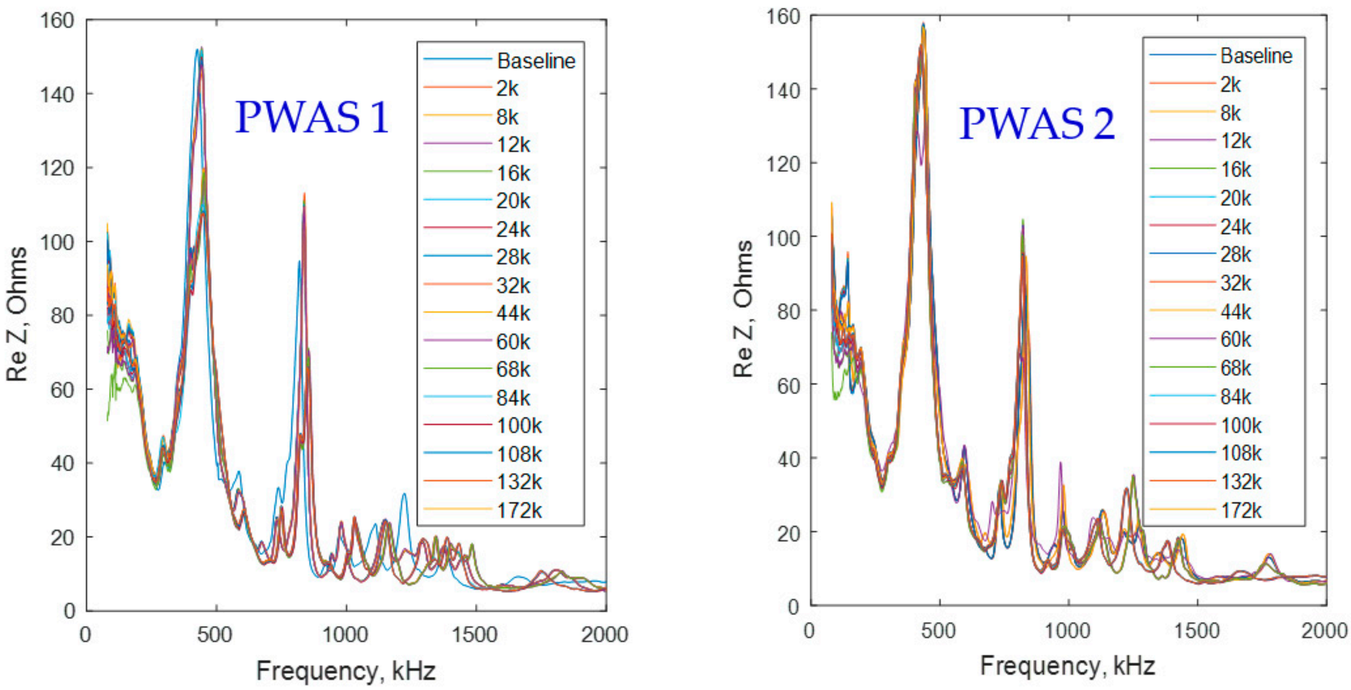

(a) (b)

Figure 7. EMIS measurement of 172 kcycles of the fatigue–crack–growth experiment. (**a**) EMIS measurement of PWAS 1 (**b**) EMIS measurement of PWAS 2. Very similar trends of EMIS spectrograms were observed during 172 kcycles. This confirmed that the PWAS bonding was in good condition during the fatigue–crack–growth experiment.

3. AE Experiment Results and Discussion

3.1. SIF Controlled vs. Load-Controlled Experiment

During a fatigue fracture activity, the SIF at the crack tip is an important governing factor. In fracture mechanics, fracture and fatigue problems encountered have been characterized using the SIF, K. An increase in K at the crack tip causes an increase in net section stress ahead of the crack. Many researchers have performed experimental as well as theoretical studies on SIF at the crack tips. Digital image correlation (DIC) has been used for the measurement of SIF experimentally [46]. Many researchers have explored the empirical formulations for calculations of SIF. The crack-tip SIF solution for the finite M(T) specimen (similar to the present specimen discussed in Section 2.1) is given by Fedderson [47] as follows.

$$K_{\text{inf}} = \sigma_{\text{inf}}\sqrt{\pi a}\sqrt{\sec(\frac{\pi a}{w})} \tag{2}$$

where σ is the far-field stress, 'a' is the crack length, and 'w' is the width of the plate (103 mm). Many researchers have found the empirical formulation by Fedderson to be very closely matching with the experimental observations [48]. The stress intensity factor at the crack tips increases with an increase in crack length if the far field stress due to the external loading is the same, as we understand from Equation (1).

According to Paris' law [49], the crack growth rate is proportional to the SIF excursion at the crack tips during a cyclic fatigue loading, i.e.,

$$\frac{da}{dN} = C\Delta K^{m} \tag{3}$$

where 'a' is the crack length, 'N' is the number of fatigue cycles, ΔK is the SIF excursion during fatigue loading, and 'C' and 'm' are arbitrary constants. We can understand that the SIF increases non-linearly with crack advancement from Equation (1) for a load-controlled experiment (where the maximum and minimum load remains the same throughout the fatigue crack growth experiment). According to Equation (2), the crack growth rate also increases theoretically due to the increment in SIF. Analogously, the increment in the crack growth rate with crack advancement was observed during the fatigue experiments we have performed. A load-controlled fatigue experiment was performed on a similar specimen discussed in Section 2.1, with a cyclic fatigue load of 13.85 kN–1.38 kN (R = 0.1). The crack grew until 20 mm tip-to-tip length was achieved. The crack length, load vs. kcycles (fatigue cycle represented in kilocycles) for the load-controlled experiment is presented in Figure 8a. When the excursion in the load remained the same during the fatigue experiment, the crack length was observed to grow non-linearly. The theoretical SIF at the crack tip was calculated, which increased non-linearly with kcycles (Figure 8b). The crack growth rate calculated from the experiment is presented in Figure 8c. The crack growth rate was also observed to grow exponentially, which is congruent with the theoretical interpretations from Equations (1) and (2). In the present experiment, the SIF at the crack tip and the crack growth rate was decided to be controlled for providing a similar environment for the AE signal generation at different crack lengths. Due to the above reasons, a novel SIF-controlled fatigue experiment was developed and presented in this paper.

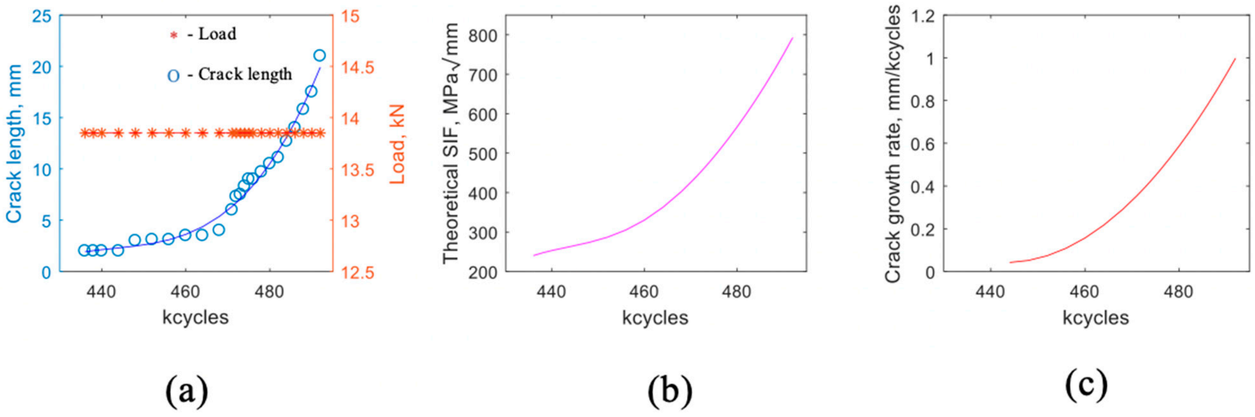

Figure 8. Load-controlled fatigue-experiment results: (**a**) fatigue kcycles vs. crack length and load; (**b**) fatigue kcycles vs. SIF; (**c**) fatigue kcycles vs. crack growth rate.

Equation (2) interprets that the crack growth rate is proportional to the SIF-excursion's exponential power in the stress intensity factor (SIF) during the loading cycle. To perform a controlled-AE experiment, by controlling the crack growth rate, the stress intensity factor at the crack tips was controlled when the crack grew in the present experiment. The novel experimental methodology is named "SIF-controlled fatigue experiment." A block diagram of the "SIF-controlled fatigue experiment" procedure is shown in Figure 9. The stress intensity factor corresponding to a load of 13.85 kN and a crack length of 2 mm tip to tip according to Equation (1) was calculated as 238 MPa$\sqrt{\text{mm}}$. The excursion in SIF (ΔK) corresponding to the excursion in the load between minimum load (1.38) and maximum load (13.85 kN) (R = 0.1) was 214 MPa$\sqrt{\text{mm}}$. When the crack grows under constant load, the maximum value of SIF at the crack tips corresponding to maximum load increases with crack length. The excursion in the SIF when the load increases from minimum to maximum load also increases according to Equation (1). In the SIF controlled experiment, for the excursion in the crack-tip SIF to be controlled with the crack growth, a new load was calculated every time with a 1 mm increment in crack length to maintain the excursion in the SIF as 214 MPa$\sqrt{\text{mm}}$, by maintaining R = 0.1 for the minimum and maximum load.

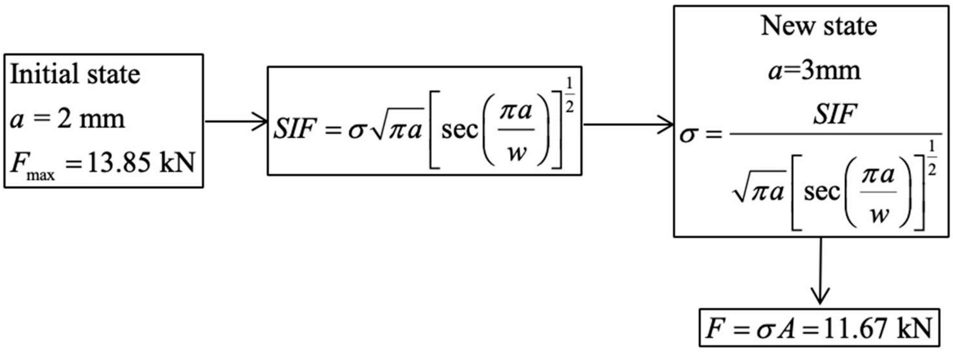

Figure 9. Block diagram for the SIF controlled fatigue experiment loading protocol. When the crack length increases by 1 mm, the new recalculated load was applied for fatigue crack growth.

The crack length vs. load plot was obtained using the protocol in Figure 9 and is presented in Figure 10. For maintaining the SIF-excursion and crack growth rate in control during the experiment, theoretically, one needs to reduce the load as the fatigue crack grows, as presented in Figure 10.

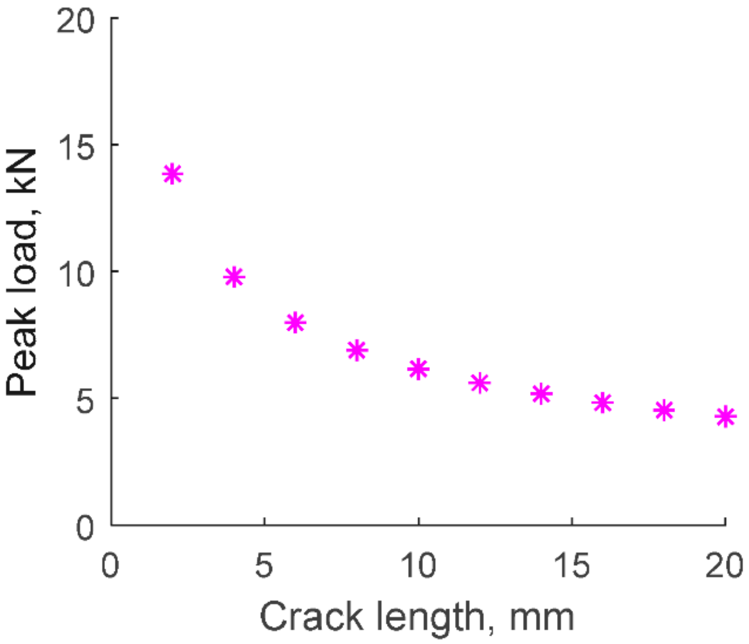

Figure 10. Load prediction for the constant-SIF crack growth experiment.

In the present experiment for AE capture, the fatigue loading was taken according to the “SIF-controlled” theory load values.

3.2. SIF Controlled Experiment AE Capture

After installing the sensors, the “SIF-controlled” fatigue loading continued to grow the crack and simultaneously capture AE signals. The fatigue crack growth experiment was continued at a frequency of 2 Hz while capturing the AE signals. The coupling of the PWAS sensor to the specimen was tested using EMIS and pencil lead break tests performed periodically. Periodic pencil lead break experiments also tested the coupling of the S9225 sensor. The fatigue loading was decreased when the crack length was progressed to control the stress intensity factor (SIF) at the crack tips and control the crack growth rate. The crack length was measured using eddy current method. The history of maximum fatigue loading applied vs. the additional number of cycles after 322 kcycles is presented in Figure 11. In this experiment, an additional 188 kcycles of fatigue loading were performed. The history of crack length measured during the fatigue experiment vs. the additional number of cycles is presented in Figure 12. From the crack length plot, one could understand that the increment in the crack length was continuously decreased, and no crack increment was observed after a certain number of cycles. From the crack length measurements, the crack growth rate was calculated and is presented in Figure 13. We observed a continuous decrement in the crack growth rate with the additional cycles after 322 kcycles. After 150 kcycles, we observed the calculated crack growth rate to be near zero.

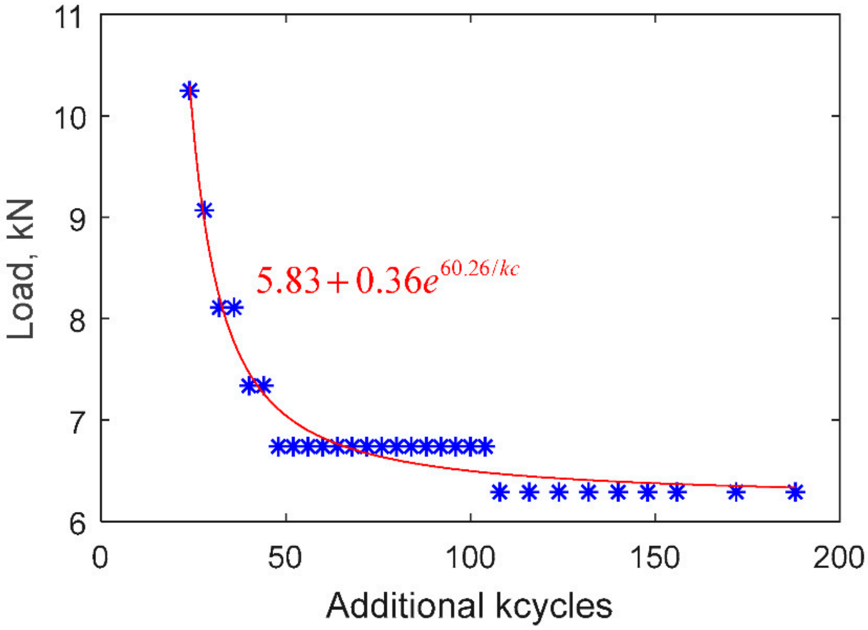

Figure 11. The load adjustment history with fatigue cycles.

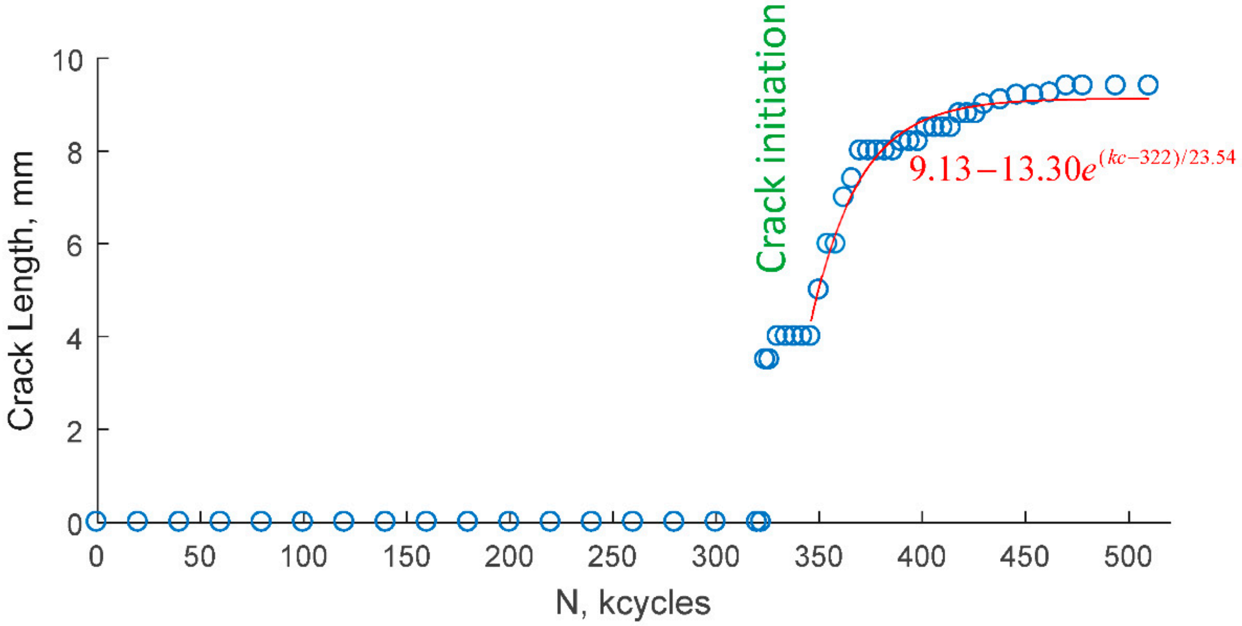

Figure 12. Fatigue crack growth during the experiment.

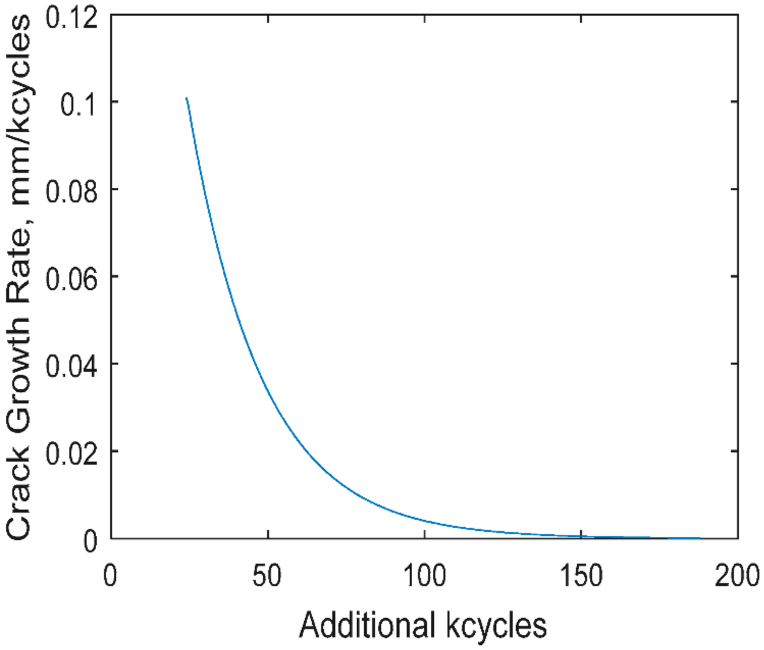

Figure 13. The crack growth rate calculated from the fatigue crack fitted curve.

In this experiment, the fatigue loading was applied to the specimen according to the SIF-controlled theory load values. The non-reflective clay boundaries were used on the specimen for obtaining boundary reflection-free AE signals during the experiment. The continuous decrement in the crack growth rate could be due to the extra damping caused by clay boundaries to the crack growth rate during the actual experiment. The crack growth rate was not observed to decrease in the experiment performed without clay boundaries [50]. Secondly, SIF theoretical formulation is an approximation to the specimen's ideal case; variations in the actual experiment are possible. These could be the reasons for the crack growth rate reducing gradually to zero.

Due to the gradual reduction in the crack growth rate, the AE signals recorded consisted of signals captured during crack growth incidents below crack growth rate 0.1 mm/kcycles. The crack growth rate progressively reduced from 0.1 mm/kcycles to zero mm/kcycles as the crack grew. Such an experiment would provide the application limit of this high cycle fatigue experiment limit to a range of crack growth rates ranging from 0.1 mm/kcycles to slowly degraded to a situation where negligible crack growth happens. Towards the end of the cycles (188 additional kcycles), the crack length was stagnant from the visual inspection. The verification of the visual inspection was performed by eddy current crack length measurement. The eddy current crack length measurement was performed before 172 kcycles and after finishing 188 additional kcycles. The eddy current measurements confirmed that no crack growth happened during this phase. AE signals were still recorded during these cycles. This stagnant crack growth situation recorded the AE signals due to the rubbing/clapping of crack faying surfaces.

In short, the present experimental setup had two important advantages. (1) The present high cycle fatigue experiment was the most appropriate representation of a real high cycle fatigue experiment because the crack growth rate during the experiment was reduced from 0.1 mm/kcycles to zero mm/kcycles. (2) Distinguishing between fatigue-crack "growth"-related AE signals and fatigue-crack "rubbing/clapping" is easily possible from the experimental design. The experiment had an active crack growth stage at the beginning of the additional fatigue cycles when the fatigue-crack-growth-related AE signals were recorded. The experiment also had an inactive crack growth stage towards 172–188 additional kcycles, when the fatigue-crack "rubbing/clapping"-related AE signals were recorded.

A large number of AE hits were observed after 48 kcycles. The reason for a large number of AE signals could be due to the formation of a favorable faying surface for rubbing/clapping within the crack during 44–48 kcycles. The two surfaces on the two sides of the crack rub and clap each other when the cyclic loading happens and continuously produce AE signals after a favorable crack faying surface was formed. The majority of the crack growth happened below 48 kcycles. During 48–188 kcycles, very little crack growth occurred compared to the first additional 48 kcycles. However, a massive number of AE hits compared with the initial cycles was observed during the later cycles. This observation asserts the following conclusions. First, the crack growth and the number of AE hits observed may not be proportional to each other during a fatigue crack growth experiment. The AE hits may be due to rubbing and clapping of the crack faying surfaces, which essentially does not cause any crack growth. Secondly, AE signal signatures exist which originate from the crack growth event and crack rubbing/clapping event. The crack growth AE signature is valuable for understanding the crack growth during the fatigue experiment. Additionally, the crack rubbing/clapping signature is useful for understanding the crack's existence, which can potentially generate due to a fatigue loading in the cracked structure or strong vibrations on the structure.

Due to the above reasons, it is vital to distinguish the AE signals recorded during the fatigue crack growth incident. Many researchers used several statistical features of the AE signals such as amplitude, energy, duration, counts, rise time, etc. for automated signal clustering and classifications [51–53]. In this research, we have used the frequency content study of the signals for the signal classification. Time-frequency domain separation of the signal was also performed to study the Lamb wave nature of the AE signals in thin metallic plates and understand the Lamb wave modes in the AE signals.

Figure 14 presents the fatigue crack growth rate vs. the additional fatigue cycles. The fatigue crack growth rate plot is superimposed with representative AE signal signatures received during the cyclic fatigue AE experiment. Additionally, the crack length (CL) and the additional fatigue cycle at which the AE signal was received is also presented in the figure. Based on the frequency spectrum observed, AE signals have been classified into two categories: first, the type-1 (T1) signature corresponding to a fatigue crack growth process and second, the type-2 (T2) signature corresponding to a fatigue crack rubbing/clapping process. In Figure 14, the signals which are under the T1 signal category is marked as T1 in green letters, and those under T2 is marked as T2 in blue letters. A confirmation of the T1 and T2 AE signals were originating from the crack was performed by AE source localization using the time of arrival of the signals at the sensors. The time of arrival at various sensors was analyzed for confirmation. Two PWAS sensors and two S9225 sensors were installed on the specimen (Figure 2) numbered PWAS-1, PWAS-2, S9225-1 and S9225-2, respectively. PWAS-1 and S9225-1 are the closest to the crack, at a distance of 6 mm. PWAS 2 and S9225-2 are at a distance of 25 mm from the crack. The relative time of arrival and amplitudes of T1 and T2 AE signals obtained from the MISTRAS AE system are presented in Tables 1 and 2. The observed arrival time and arrival sequence are possible only if the AE signal origin is at the crack. This analysis confirms that the T1 and T2 AE signals originate from the crack.

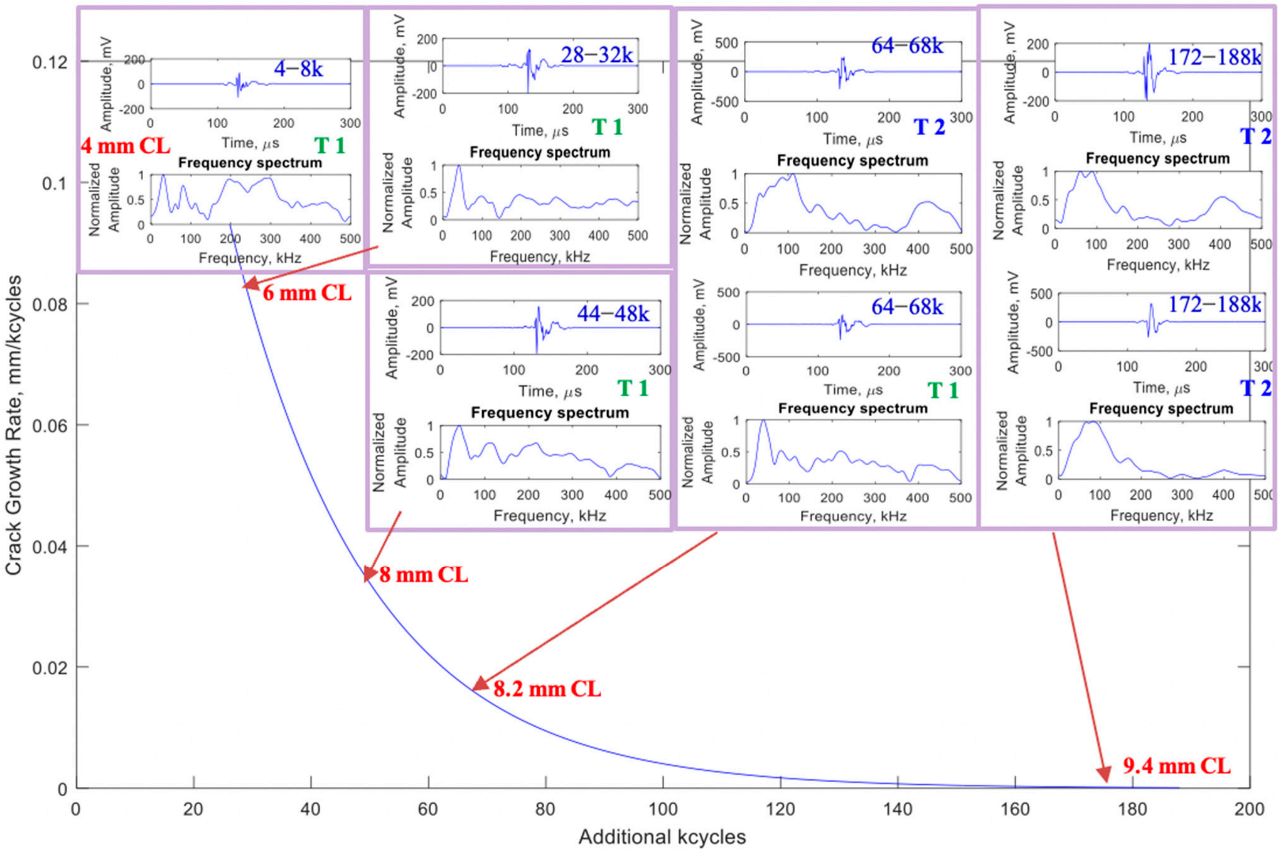

Figure 14. AE signal signatures recorded using PWAS–1 during additional fatigue cycles after crack growth. The fatigue crack growth rate plot is superimposed with representative AE signal signatures received during the cyclic fatigue AE experiment.

Table 1. Time of arrival and sequence of arrival of T1 AE signals at various Sensors. PWAS-1 and S9225-1 are the closest to the crack. Hence, AE signals first arrive at PWAS-1 and S9225-1. PWAS 2 and S9225-2 are at 25 mm from the crack. Hence, AE signals arrive approximately at the same time at PWAS-2 and S9225-2. This analysis confirms that AE signals are originating from the crack.

	Time of Arrival (TOA), µs (Relative)	Sequence of Arrival
PWAS 1	32	1
S9225 1	34	2
PWAS 2	36	3
S9225 2	37	4

Table 2. Time of arrival and sequence of arrival of sampe T2 AE signal at various Sensors. PWAS-1 and S9225-1 are the closest to the crack. Hence, AE signals first arrive at PWAS-1 and S9225-1 approximately at same time. PWAS 2 and S9225-2 are at 25 mm from the crack. Hence, AE signals arrive approximately at the same time at PWAS-2 and S9225-2. This analysis confirms that AE signals originate from the crack.

	Time of Arrival (TOA), µs (Relative)	Sequence of Arrival
PWAS 1	76	1
S9225 1	78	2
PWAS 2	82	3
S9225 2	83	4

Analysis of T1 and T2 AE signal signatures was performed to identify the characteristics of the signatures. The signature T1 was observed to have a broadband frequency spectrum, as we find in Figure 14. On the other hand, the signature T2 was observed to have two major peaks in the frequency spectrum (50–150 kHz and 400–500 kHz) and a valley between 200 to 400 kHz. The strength of the peak between 400–500 kHz for T2 was observed to have variations as we observe in the figure.

Signature T1 was more frequent before 44 kcycles when active crack growth was happening. The total number of T1 signatures, which were recognized from the analysis, is 17. After 44 kcycles, T2 was observed to be more frequent. Referring to Figure 14, we could understand that the majority of crack growth happened during cycles before 44 kcycles (4 to 8 mm crack growth). It is hypothesized that after 44 kcycles, a favorable crack faying surface for generation of rubbing/clapping AE signal was formed, and this produced AE signals due to rubbing/clapping even in the absence of crack growth. The number of T2 AE hits were so large that it was not of interest to count them all, at least for this initial exploratory study. In fact, in each fatigue cycles, the crack surfaces were rubbing/clapping and producing T2 AE hits. In conclusion, the T1 signature could be due to a fatigue crack growth process, and the T2 signature could be due to a fatigue crack rubbing/clapping process due to the above reasons.

To study further the characteristics of T1 and T2 signal signatures, a time-frequency analysis of the signals was performed. The Choi–Williams transform of the AE signals at PWAS 2 (25 mm from the crack) was performed for time-frequency analysis. The time-frequency plot of a T1 AE signal has been presented in Figure 15. The group velocity dispersion curve of S0 and A0 Lamb wave modes is overlapped with the time-frequency plot to identify the Lamb wave mode content in the AE signal. For the T1 signature, we observe a strong S0 Lamb wave mode content presence in the signal. The time frequency analysis of T2 signature is also presented in Figure 16. For the T2 signature, A0 Lamb wave mode content was observed to be stronger as we observe in Figure 16b. Hence, the major difference between the T1 crack growth AE and T2 crack rubbing/clapping AE is that the crack-growth-related AE has stronger S0 Lamb wave mode content, and the latter have stronger A0 Lamb wave mode content.

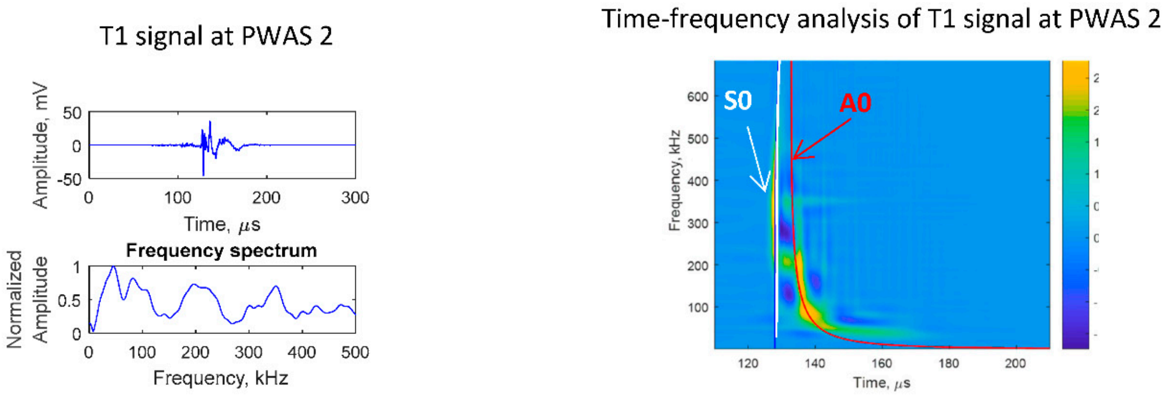

(a)

(b)

Figure 15. Time-frequency analysis of T1 AE signal at PWAS–2: (**a**) T1 signal at PWAS–2; (**b**) Choi–Williams transform of the T1 signal at PWAS–2. A strong S0 Lamb wave mode was observed for the T1 signal at PWAS–2.

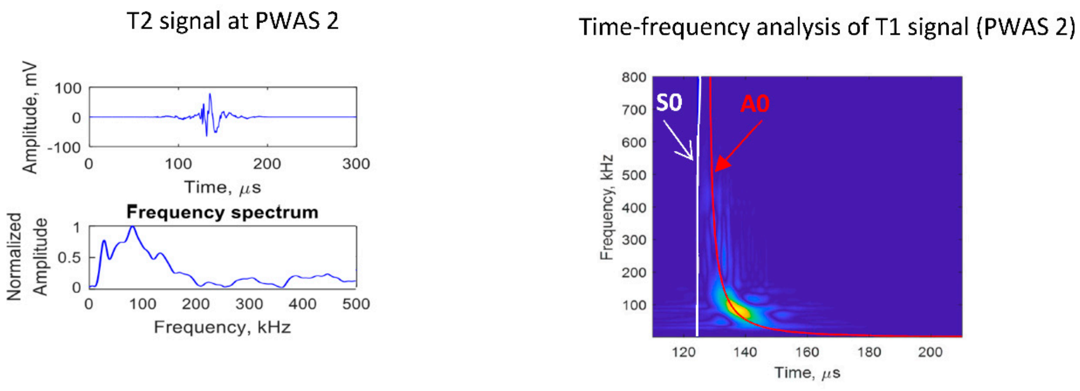

(a)

(b)

Figure 16. The time–frequency analysis of T2 AE signal at PWAS 2. (**a**) T2 signal at PWAS–2; (**b**) Choi–Williams transform of T2 signal at PWAS–2. A strong A0 Lamb wave mode content was observed for the T2 signal at PWAS–2.

We have also used S9225 AE sensors for the detection of AE signals. A comparison of AE signal signatures T1 and T2 at PWAS-1 and S9225-1 are shown in Figure 17. We observe S9225 sensor responses have a strong response at the low-frequency range (30–150 kHz). The response above the 150 kHz range is found very poor.

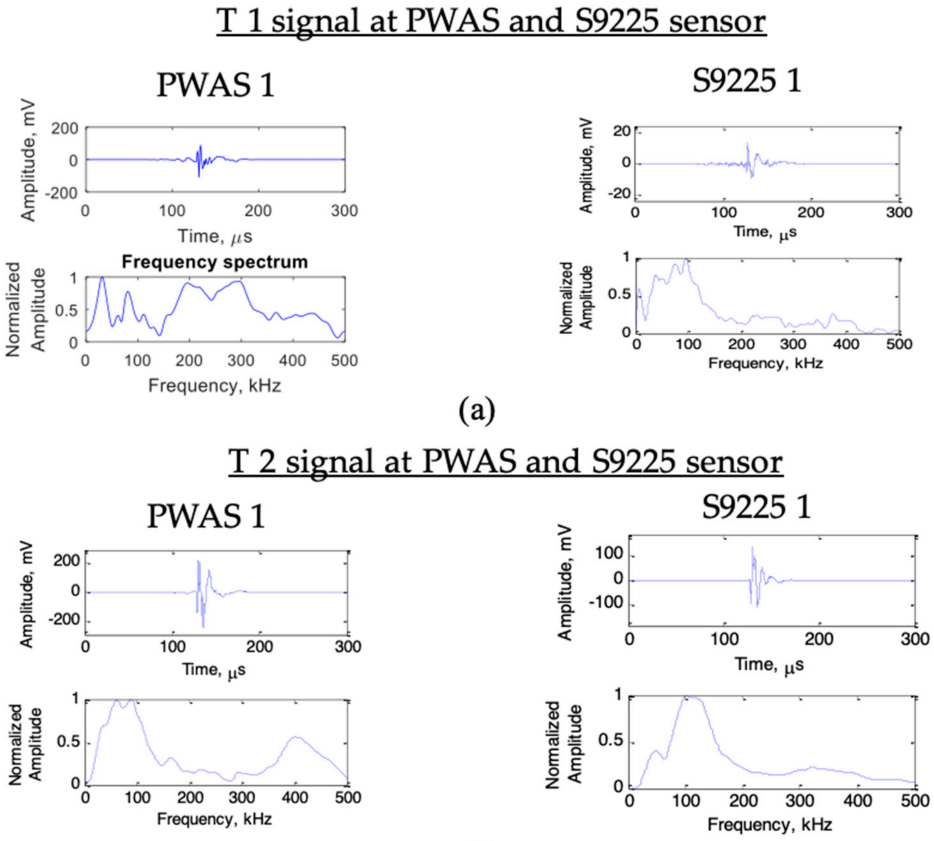

(a)

(b)

Figure 17. Comparison of T1 and T2 signature at PWAS and S9225 sensors. (**a**) T1 signature at PWAS–1 and S9225–1. (**b**) T2 signature at PWAS and S9225.

The repeatability of the AE signals was inspected by performing another similar experiment with an identical specimen. The comparison of the T1 AE signal signature and T2 AE signal signature recorded using the specimen-1 and specimen-2 is presented in Figure 18. The signal received at PWAS 2 is also presented in the figure. We observe a fast-traveling wave packet marked with a blue oval and a slow-traveling wave packet marked with a red oval in T1 signals recorded using specimen-1 and specimen-2. The signal frequency spectrum was also observed as broadband for both T1 signals recorded using specimen-1 and specimen-2. Whereas T2 signature recorded using both specimens were observed to have only one major wave packet. Additionally, both the signals had two major peaks in the frequency spectrum: the first one at 50–150 kHz and the second one at 400–500 kHz. The results obtained from both the specimens proved the repeatability of the experiment.

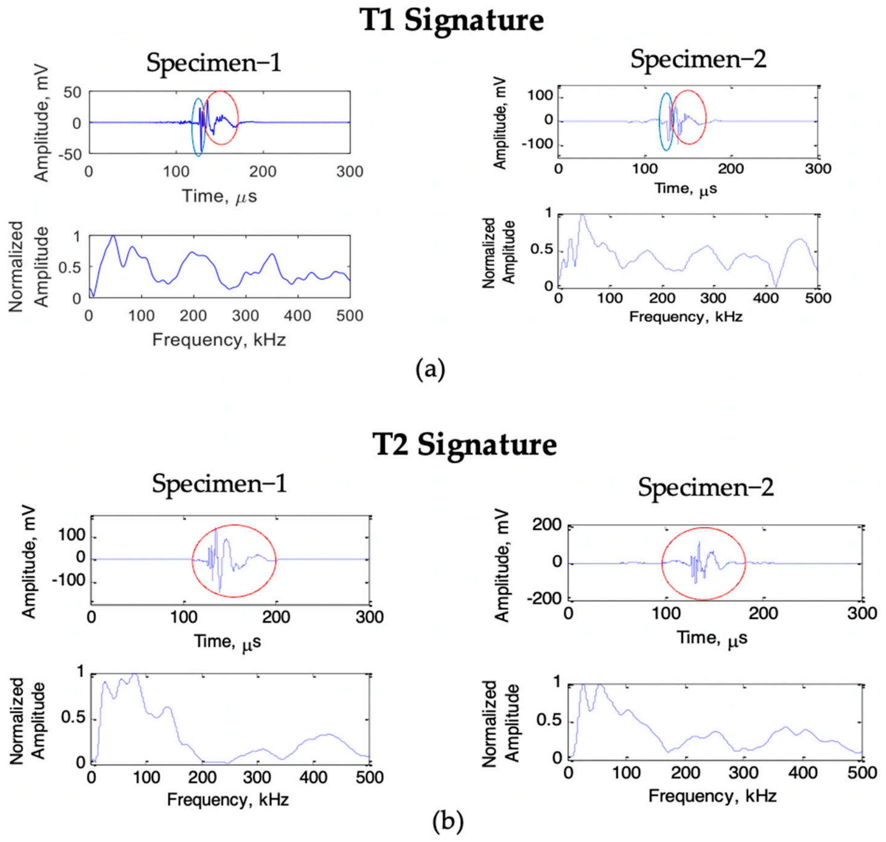

Figure 18. The repeatability assessment of T1 and T2 AE signal signatures. Another specimen with the same aluminum 2024–T3 material was tested under fatigue loading and compared with the present experimental results. A close match of results was observed. (**a**) T1 signature in specimen 1 and specimen 2 at PWAS–2: separation of two wave packets is visible in both signals; (**b**) T2 signature in specimen 1 and specimen 2 at PWAS–2: only the single wave packet is visible in both signals; similar peaks and valleys are observed.

Pearson Correlation Clustering (PCC) of AE Signals

During the fatigue experiment, due to fatigue crack growth and crack rubbing and clapping of crack faying surfaces, a large number of AE signals would be generated. It is a large amount of data, and an effective method for comparison of AE signals need to be developed. In this work, we have implemented the Pearson correlation coefficient (PCC) method for the characterization and clustering of the AE signals. The Pearson correlation coefficient between two continuous variables is the test statistics that measure the statistical relationship or association between two continuous variables. Since it is based on the method of covariance, it is known as the best method of measuring the association between variables of interest. It gives information about the magnitude of the association, or correlation, as well as the direction of the relationship.

A particular signal is chosen as the base signal, and all other signals are correlated to the base signal to obtain the correlation coefficient value. It is recommended to choose the strongest signal (highest amplitude signal) among the AE signals as the base signal to have a good SNR (signal to noise ratio) for the base signal. For two time-domain/ frequency domain AE signals, cross-correlation of the signals was performed to adjust the time delay between the signals. Later on, the signals were normalized before performing correlation. Using the following expression [45,54], a correlation coefficient is calculated.

$$\rho(A,B) = \frac{1}{N-1}\sum_{i=1}^{N}\left(\frac{A_i-\mu_A}{\sigma_A}\right)\left(\frac{B_i-\mu_B}{\sigma_B}\right) \tag{4}$$

where A_i = time domain signal A, B_i = time domain signal B, μ_A = mean of signal A, μ_B = mean of signal B, σ_A = standard deviation of signal A, and σ_B = standard deviation of signal B. Two separate correlation coefficients were calculated, using time domain as well as frequency domain data. Two-dimensional scatter plots of time-domain PCC vs. frequency domain PCC were constructed. A detailed flow chart of obtaining correlation coefficient is presented in Figures 19 and 20.

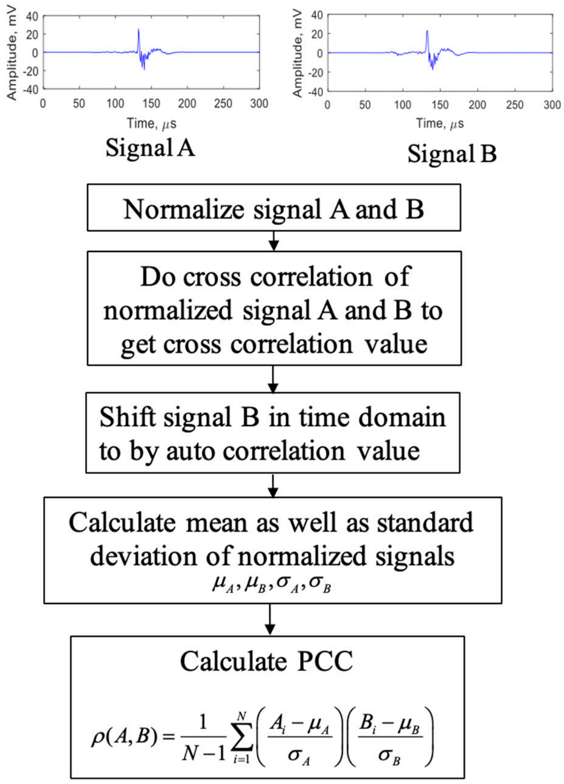

Figure 19. Procedure for obtaining the Pearson correlation coefficient of two time–domain signals.

Using the Pearson correlation method, the clustering of fatigue crack growth (T1) and fatigue crack rubbing/clapping (T2) AE signals was performed. The results of the Pearson correlation method are presented in Figure 21. Seven fatigue crack growth signals and seven fatigue crack rubbing/clapping signals (From 172–178 additional kcycles) were considered for the analysis. The signal in Figure 21b is the base signal for the correlation analysis. As we observe from the figure, two AE signal clusters were formed, first the fatigue crack growth signal cluster and second the fatigue crack rubbing/clapping signal cluster. The two clusters are separated by two ovals in Figure 21a. The fatigue crack growth signal cluster is found to be a loose cluster because the fatigue crack growth signal consists of AE signals at different crack lengths. The fatigue crack rubbing/clapping cluster is found to form a tight cluster. For the T1 cluster, the time domain correlation values of the signals were observed between 0.25 and 0.55 and the frequency correlation is observed between 0.55 and 0.8. However, for the crack rubbing/clapping signals, the time and frequency correlation values were observed between 0.9 and 1. Two representative signals from each cluster have been presented with arrow marks corresponding to the location of the signal in the Pearson correlation scatter plot. Thus, the novel statistical method has proved that the fatigue crack growth and fatigue crack rubbing/clapping signals are two groups and it is possible to distinguish them using this novel statistical method.

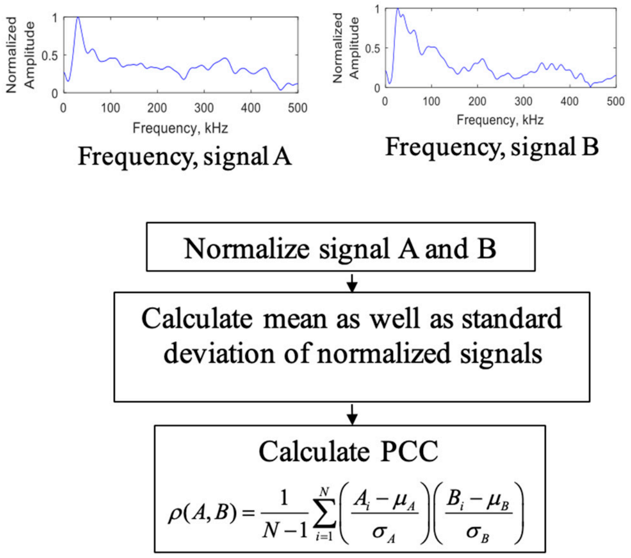

$$\rho(A,B)=\frac{1}{N-1}\sum_{i=1}^{N}\left(\frac{A_i-\mu_A}{\sigma_A}\right)\left(\frac{B_i-\mu_B}{\sigma_B}\right)$$

Figure 20. Procedure for obtaining the Pearson correlation coefficient of frequency spectra of two time-domain signals.

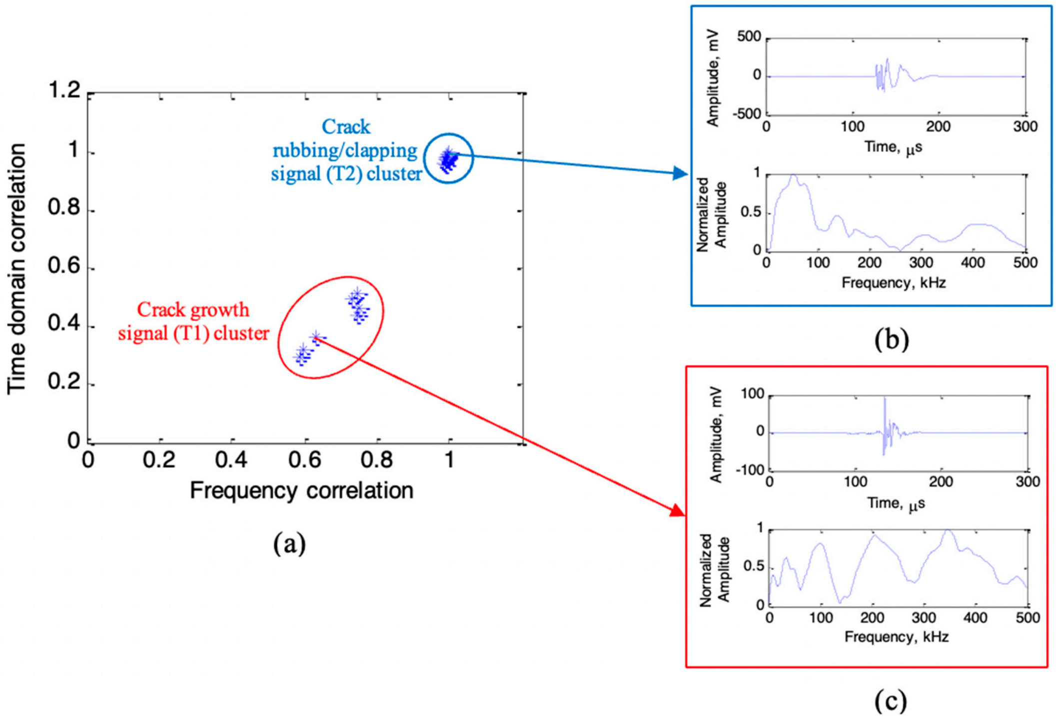

Figure 21. Clustering of fatigue crack growth (T1) and fatigue crack rubbing/clapping (T2) AE signals during fatigue experiment using the Pearson correlation method. (**a**) Pearson correlation plot; (**b**) representative signal from T2 cluster; (**c**) representative signal from the T1 cluster.

4. Summary and Conclusions

4.1. Summary

A new SIF-controlled HCF experimental design was proposed and performed in this manuscript for fatigue-crack AE signal identification and classification. In this novel experimental design, the SIF at the crack-tip was controlled by reducing the load with an increase in crack length. The load levels were adjusted to control the SIF at the crack tips such that the crack growth was slowed down and even inhibited at certain crack length. The load levels for the test were chosen according to the load levels calculated from the SIF theory. A continuously slowing down crack-growth-rate was observed, and the AE signals during the crack growth rate from 0.1 mm/kcycles to inhibited crack growth were recorded. The crack was allowed to grow up to 9.4 mm crack length during the experiment. AE signals were still recorded even after the crack stopped growing. The arrival time at the AE sensors ensured that the AE signals from the non-crack-growth situation were from the crack. After 172 additional fatigue cycles post fatigue crack initiation, no crack growth was observed during 16 kcycles while AE signals were still being captured. Fatigue crack rubbing/clapping AE signals were recorded from these 16 kcycles (172–188 kcycles). Further analysis of the AE signals recorded was performed by Fast Fourier Transform (FFT) and Choi–Williams Transform (CWT) analysis to classify the AE signals. We identified that the AE signals related to fatigue crack growth are different from the fatigue crack rubbing/clapping AE signals. In this study, novel Pearson correlation analysis was also used for classification and clustering of AE signals.

4.2. Conclusions

A continuously decaying fatigue crack growth rate can be achieved from the present novel experimental load design of the SIF-controlled HCF fatigue experiment. From the experimentally observed AE signals, two broad classes of AE signal signatures were identified based on the AE signal analysis. The signal signature classes were named T1 and T2. The T1 signature has a broadband characteristic in the frequency spectrum, whereas T2 has two major peaks at 50–150 kHz and 400–500 kHz and a valley at 200–400 kHz in the frequency spectrum corresponding to the A0 Lamb wave mode tuning of 7 mm PWAS on a 1 mm aluminum plate. For the T1 signature, strong S0 Lamb wave mode content was observed, whereas the T2-signature had strong A0 mode content based on the Lamb wave mode separation study performed using CWT. T1-signature AE signals were recorded frequently during the fatigue crack growth stage, and T2-signature AE signals were frequently recorded during the non-crack growth stage. No T1-signature was observed when the crack was not growing. This research identified that the T1-signature is due to the fatigue crack growth event because of the above reason. It was also identified that the non-crack growth AE signals are originating from fatigue crack rubbing/clapping during the fatigue crack cyclic loading, causing the generation of the T2 AE signal signature. Novel Pearson correlation analysis could classify the T1 and T2 signals.

Author Contributions: In this article, the detailed methodology was provided by V.G. and R.J.; The formal analysis was done by R.J.; R.J. prepared the original draft; review and editing were done by V.G. and R.J.; All authors have read and agreed to the published version of the manuscript.

Funding: This work was supported by the Office of Naval Research (ONR), grant number N00014-21-1-2212.

Institutional Review Board Statement: Not applicable.

Informed Consent Statement: Not applicable.

Data Availability Statement: Not applicable.

Conflicts of Interest: The authors declare no conflict of interest.

References

1. Zhang, L.; Ozevin, D.; Hardman, W.; Timmons, A. Acoustic Emission Signatures of Fatigue Damage in Idealized Bevel Gear Spline for Localized Sensing. *Metals* **2017**, *7*, 242. [CrossRef]
2. Roberts, T.M.; Talebzadeh, M. Acoustic emission monitoring of fatigue crack propagation. *J. Constr. Steel Res.* **2003**, *59*, 695–712. [CrossRef]
3. Morton, T.M.; Harrington, R.M.; Bjeletich, J.G.; Palo, L.; Alto, P. Acoustic emissions of fatigue crack growth. *Eng. Fract. Mech.* **1973**, *5*, 691–697. [CrossRef]
4. Deschanel, S.; Rhouma, W.B.; Weiss, J. Acoustic emission multiplets as early warnings of fatigue failure in metallic materials. *Sci. Rep.* **2017**, *7*, 13680. [CrossRef] [PubMed]
5. Roberts, T.M.; Talebzadeh, M. Fatigue life prediction based on crack propagation and acoustic emission count rates. *J. Constr. Steel Res.* **2003**, *59*, 679–694. [CrossRef]
6. Keshtgar, A.; Modarres, M. Acoustic Emission-Based Fatigue Crack Growth Prediction. In Proceedings of the 2013 Proceedings Annual Reliability and Maintainability Symposium (RAMS), Orlando, FL, USA, 28–31 January 2013; pp. 1–5.
7. Shen, Y.; Wang, J.; Xu, W. Nonlinear features of guided wave scattering from rivet hole nucleated fatigue cracks considering the rough contact surface condition. *Smart Mater. Struct.* **2018**, *27*, 105044. [CrossRef]
8. Bhuiyan, M.Y.; Giurgiutiu, V. The signatures of acoustic emission waveforms from fatigue crack advancing in thin metallic plates. *Smart Mater. Struct.* **2018**, *27*, 15019. [CrossRef]
9. Bhuiyan, Y.; Bao, J.; Poddar, B. Toward identifying crack-length-related resonances in acoustic emission waveforms for structural health monitoring applications. *Struct. Health Monit.* **2018**, *17*, 577–585. [CrossRef]
10. Bhuiyan, M.Y.; Giurgiutiu, V. Experimental and Computational Analysis of Acoustic Emission Waveforms for SHM Applications. In Proceedings of the 11th International Workshop on Structural Health Monitoring, Stanford, CA, USA, 12–14 September 2017; pp. 1–7.
11. Hamstad, M.A.; McColskey, J.D. Detectability of slow crack growth in bridge seels by acoustic emission. *Mater. Eval.* **1998**, *1165*, 57–1174.
12. Wisner, B.; Mazur, K.; Perumal, V.; Baxevanakis, K.P.; An, L.; Feng, G.; Kontsos, A. Acoustic emission signal processing framework to identify fracture in aluminum alloys. *Eng. Fract. Mech.* **2018**, *210*, 367–380. [CrossRef]
13. Carpinteri, A.; Lacidogna, G.; Niccolini, G.; Puzzi, S. Critical defect size distributions in concrete structures detected by the acoustic emission technique. *Meccanica* **2008**, *43*, 349–363. [CrossRef]
14. Farhidzadeh, A.; Salamone, S. Introducing Sifted b-Value Analysis and a New Crack Classification for Monitoring Reinforced Concrete Shear Walls by Acoustic Emission. In Proceedings of the 54th Meeting of Acoustic Emission Working Group Meeting (AEWG), Princeton, NJ, USA, 20–23 May 2012; Volume 1, pp. 55–57.
15. Ohno, K.; Ohtsu, M. Crack classification in concrete based on acoustic emission. *Constr. Build. Mater.* **2010**, *24*, 2339–2346. [CrossRef]
16. Farhidzadeh, A.; Salamone, S.; Dehghan-Niri, E.; Luna, B.; Whittaker, A. Damage Assessment of Reinforced Concrete Shear Walls by Acoustic Emission. *Struct. Mater. Technol.* **2012**, *2014*, 74–81.
17. Poddar, B.; Giurgiutiu, V. Experimental Validation of Analytical Model for Lamb Wave Interaction with Geometric Discontinuity. In Proceedings of the SPIE 9437, Structural Health Monitoring and Inspection of Advanced Materials, Aerospace, and Civil Infrastructure 2015, San Diego, CA, USA, 8–12 March 2015; p. 94371Y.
18. Shen, Y.; Giurgiutiu, V. Effective non-reflective boundary for Lamb waves: Theory, finite element implementation, and applications. *Wave Motion* **2015**, *58*, 22–41. [CrossRef]
19. Ohtsu, M.Y.; Ono, K. A generalized theory of acoustic emission and Green's functions in a half Space. *J. Acoust. Emiss.* **1984**, *1984*, 27–35.
20. Ohtsu, M.; Ono, K. The generalized theory and source representations of acoustic emission. *J. Acoust. Emiss.* **1986**, *1986*, 124–133.
21. Hamstad, M.A.; O'Gallagher, A.; Gary, J. Modeling of buried monopole and dipole sources of acoustic emission with a finite element technique. *J. Acoust. Emiss.* **1999**, *17*, 97–110.
22. Prosser, W.H.; Hamstad, M.A.; Gary, J.; O'gallagher, A. Finite Element and Plate Theory Modeling of Acoustic Emission Waveforms. *J. Nondestruct. Eval.* **1999**, *18*, 83–90. [CrossRef]
23. Sause, M.G.R.; Hamstad, M.A.; Horn, S. Finite element modeling of lamb wave propagation in anisotropic hybrid materials. *Compos. Part B Eng.* **2013**, *53*, 249–257. [CrossRef]
24. Sause, M.G.R.; Richler, S. Finite element modeling of cracks as acoustic emission sources. *J. Nondestruct. Eval.* **2015**, *34*, 4. [CrossRef]
25. Wisner, B.; Kontsos, A. Investigation of particle fracture during fatigue of aluminum 2024. *Int. J. Fatigue* **2018**, *111*, 33–43. [CrossRef]
26. Wirtz, S.F.; Beganovic, N.; Söffker, D. Investigation of damage detectability in composites using frequency-based classification of acoustic emission measurements. *Struct. Health Monit.* **2019**, *18*, 1207–1218. [CrossRef]
27. Hamdi, S.E.; Le Duff, A.; Simon, L.; Plantier, G.; Sourice, A.; Feuilloy, M. Acoustic emission pattern recognition approach based on Hilbert-Huang transform for structural health monitoring in polymer-composite materials. *Appl. Acoust.* **2013**, *74*, 746–757. [CrossRef]

28. Crivelli, D.; Guagliano, M.; Eaton, M.; Pearson, M.; Al-Jumaili, S.; Holford, K.; Pullin, R. Localisation and identification of fatigue matrix cracking and delamination in a carbon fibre panel by acoustic emission. *Compos. Part B Eng.* **2015**, *74*, 1–12. [CrossRef]
29. de Oliveira, R.; Marques, A.T. Health monitoring of FRP using acoustic emission and artificial neural networks. *Comput. Struct.* **2008**, *86*, 367–373. [CrossRef]
30. Suzuki, H.; Kinjo, T.; Hayashi, Y.; Takemoto, M.; Ono, K. Wavelet transform of acoustic emission signals. *J. Acoust. Emiss.* **1996**, *14*, 69–84.
31. Martínez-Jequier, J.; Gallego, A.; Suárez, E.; Javier, F.; Valea, Á. Real-time damage mechanisms assessment in CFRP samples via acoustic emission Lamb wave modal analysis. *Compos. Part B Eng.* **2015**, *68*, 317–326. [CrossRef]
32. Marec, A.; Thomas, J.; El Guerjouma, R. Damage characterization of polymer-based composite materials: Multivariable analysis and wavelet transform for clustering acoustic emission data. *Mech. Syst. Signal Process.* **2008**, *22*, 1441–1464. [CrossRef]
33. Ni, Q.Q.; Iwamoto, M. Wavelet transform of acoustic emission signals in failure of model composites. *Eng. Fract. Mech.* **2002**, *69*, 717–728. [CrossRef]
34. Physical Acoustics Corporation, R15a—150 kHz General Purpose AE Sensor. 2021. Available online: https://www.physicalacoustics.com/by-product/sensors/R15a-150-kHz-General-Purpose-AE-Sensor (accessed on 20 December 2022).
35. Physical Acoustics Corporation, S9225—300-1800 kHz Lightweight Miniature AE Sensor with Integral Coaxial Cable. 2021. Available online: https://www.physicalacoustics.com/by-product/sensors/S9225-300-1800-kHz-Lightweight-Miniature-AE-Sensor-with-Integral-Coaxial-Cable (accessed on 20 December 2022).
36. Perez, I.M.; Cui, H.; Udd, E. Acoustic Emission Detection Using Fiber Bragg Gratings. In Proceedings of the SPIE 4328, Smart Structures and Materials 2001: Sensory Phenomena and Measurement Instrumentation for Smart Structures and Materials, Newport Beach, CA, USA, 4–8 March 2001.
37. Mabry, N.; Banks, C.; Toutanji, H.; Seif, M. Acoustic Emission Felicity Ratio Measurements in Carbon Composites Laminates Using Fiber Bragg Grating Sensors. In Proceedings of the SPIE 7982, Smart Sensor Phenomena, Technology, Networks, and Systems, San Diego, CA, USA, 6–10 March 2011; p. 79820Y.
38. Wu, Q.; Okabe, Y. Novel Acoustic Emission Sensor System Based on Two Cascaded Phase-Shifted Fiber Bragg Gratings. In Proceedings of the SPIE 8421, OFS2012 22nd International Conference on Optical Fiber Sensors, Beijing, China, 14–19 December 2012; p. 84214H.
39. Wei, P.; Han, X.; Xia, D.; Liu, T.; Lang, H. Novel fiber-optic ring acoustic emission sensor. *Sensors* **2018**, *18*, 215. [CrossRef]
40. Joseph, R.; Bhuiyan, M.Y.; Giurgiutiu, V. Acoustic emission from vibration of cracked sheet-metal samples. *Eng. Fract. Mech.* **2019**, *217*, 106544. [CrossRef]
41. Rabiei, M.; Modarres, M. Quantitative methods for structural health management using in situ acoustic emission monitoring. *Int. J. Fatigue* **2013**, *49*, 81–89. [CrossRef]
42. Yu, J.; Ziehl, P.; Zrate, B.; Caicedo, J. Prediction of fatigue crack growth in steel bridge components using acoustic emission. *J. Constr. Steel Res.* **2011**, *67*, 1254–1260. [CrossRef]
43. Adams, D. *Health Monitoring of Structural Materials and Components: Methods with Applications*; Wiley: Hoboken, NJ, USA, 2007.
44. Simmons, J.A.; Turner, C.D.; Wadley, H.N.G. Vector calibration of ultrasonic and acoustic emission transducers. *J. Acoust. Soc. Am.* **1987**, *82*, 1122–1130. [CrossRef]
45. Giurgiutiu, V. *Structural Health Monitoring with Piezoelectric Wafer Active Sensors*; Elsevier Academic Press: Amsterdam, The Netherlands, 2014; p. 1032. ISBN 9780124186910.
46. McNeill, S.R.; Peters, W.H.; Sutton, M.A. Estimation of stress intensity factor by digital image correlation. *Eng. Fract. Mech.* **1987**, *28*, 101–112. [CrossRef]
47. Stephens, R.I. *Metal Fatigue in Engineering*; John Wiley and Sons: Hoboken, NJ, USA, 2013.
48. Chandran, K.S.R. Insight on physical meaning of finite-width-correction factors in stress intensity factor (K) solutions of fracture mechanics. *Eng. Fract. Mech.* **2017**, *186*, 399–409. [CrossRef]
49. Paris, P.C.; Gomez, M.P.; Anderson, W.E. A rational analytic theory of fatigue. *Trend Eng.* **1961**, *13*, 9–14.
50. Joseph, R. Acoustic Emission and Guided Wave Modeling and Experiments for Structural Health Monitoring and Non-Destructive Evaluation. Ph.D. Thesis, University of South Carolina, Columbia, SC, USA, 2020.
51. Gutkin, R.; Green, C.J.; Vangrattanachai, S.; Pinho, S.T.; Robinson, P.; Curtis, P.T. On acoustic emission for failure investigation in CFRP: Pattern recognition and peak frequency analyses. *Mech. Syst. Signal Process.* **2011**, *25*, 1393–1407. [CrossRef]
52. Liu, P.F.; Chu, J.K.; Liu, Y.L.; Zheng, J.Y. A study on the failure mechanisms of carbon fiber/epoxy composite laminates using acoustic emission. *Mater. Des.* **2012**, *37*, 228–235. [CrossRef]
53. Godin, N.; Huguet, S.; Gaertner, R. Integration of the Kohonen's self-organising map and k-means algorithm for the segmentation of the AE data collected during tensile tests on cross-ply composites. *NDT E Int.* **2005**, *38*, 299–309. [CrossRef]
54. Mays, L.W.; Tung, Y.-K. Uncertainty and Reliability Analysis of Hydrosystems. In *Hydrosystems Engineering and Management*; McGraw-Hill: New York, NY, USA, 1992.